8 Determining Orbital Wavefunctions using Core-Level Non-Resonant Inelastic X-Ray Scattering

Liu Hao Tjeng
Max-Planck Institute for Chemical Physics of Solids
Nöthnitzer Str. 40, 01187 Dresden

Contents

E. Pavarini, E. Koch, A. Lichtenstein, and D. Vollhardt (eds.)
DMFT: From Infinite Dimensions to Real Materials
Modeling and Simulation Vol. 8
Forschungszentrum Jülich, 2018, ISBN 978-3-95806-313-6
http://www.cond-mat.de/events/correl18

1 Introduction

The spectacular physical properties often observed in materials containing transition-metal and rare-earth elements challenge our comprehension of solid-state physics. Their properties include superconductivity, unusually large magneto-resistance, metal-insulator transitions, heavy-fermion behavior, multi-ferroicity, and phenomena involving topologically protected states. We would like to understand how the electrons in these materials interact with each other so that they generate those unusual quantum phenomena. From a theoretical point of view it is clear that the equations we have to solve are so complicated that we will not be able to obtain exact solutions. In addition, to make things worse but also more fascinating, tiny changes in temperature, pressure, or the material's composition may cause large changes of their properties. Hence, it appears that there are many solutions available that are very close in energy.

With exact solutions out of reach, the objective is then to find smart approximations by which we can capture the essential physics to describe the *correlated* motion of the electrons in such materials. Experiments are necessary to determine which aspects of the electronic and lattice degrees of freedom are the important ones. Although conceptually clean and beautiful, theoretical simplifications in terms of, for instance, a Heisenberg model or a single band Hubbard model turn out to be inadequate. It now becomes more and more clear that the interplay between the relevant charge, orbital, and spin degrees of freedom of the transition metal and rare earth ions involved determines the intricate balance between band formation and electron correlation effects. This is shown very vividly, for example, for the metal-insulator-transitions taking place in V_2O_3, $Ca_{2-x}Sr_xRuO_4$, VO_2, and Ti_2O_3 [1–8]. It may very well be that we need to develop and use different approximations for different materials or properties.

While a variety of experimental techniques are available to determine the relevant spin and charge quantum numbers, the detection of the active orbital wave functions remains a rather delicate endeavor. The standard experimental technique for $4f$ systems is inelastic neutron scattering [9–13], but the analysis of magnetic intensities is often hampered by broadened lines, phonons in the same energy window as the magnetic excitations, or strong absorption of one of the sample's constituents (e.g. Rh, In, B, or Sm). For transition metal ions, the energy scale of the local excitations is usually much too large for neutrons. Another experimental method is x-ray absorption spectroscopy on single crystals, where the polarization dependence of the dipole-allowed core-level excitations, e.g., $2p \rightarrow 3d$ or $3d \rightarrow 4f$ transitions, encodes the desired information concerning the orbital wave function [1, 2, 6, 8, 14–18].

However, this method which is based on dipolar electronic transitions has the limitation that symmetries with higher than twofold rotational symmetry cannot be detected (unless it is accompanied by a sufficiently large energy difference), e.g., for cubic systems.

We will present here the opportunities provided by a new x-ray technique, namely core-level non-resonant inelastic x-ray scattering (NIXS). This photon-in photon-out technique with hard x-rays has become feasible thanks to the high brilliance of modern synchrotrons and advanced instrumentation. The available large momentum transfers allow studying excitations that are dipole forbidden. These so-called *beyond dipole* or *multipolar* excitations contain extra infor-

mation, thus enabling us to obtain very detailed insight into the ground-state symmetry of the ion of interest. The interpretation of the spectra is straightforward and quantitative, facilitated also by the fact that the multipolar excitations are more excitonic than the dipole ones. Experimentally, NIXS comes also with the advantage that it is a bulk sensitive technique thanks to the large penetration depth of the hard x-rays used, meaning that there is no need to use ultra-high vacuum or special surface preparation procedures as commonly employed in more surface sensitive probes like soft-x-ray absorption or photoelectron spectroscopies. With the hard x-ray beams typically having a spot size of 50 µm or smaller, NIXS allows also the measurement of much smaller samples than typically required for neutron experiments. In addition, NIXS is suitable for high pressure experiments, pressure being an important tuning parameter when studying phase diagrams.

We will discuss our case for the example of SmB_6, a material currently under intense investigation because of the expectation that it may be the first strongly correlated system that has non-trivial topological properties. The manuscript is organized as follows: We first describe the basic principles of the spectroscopic method NIXS. We then apply the method to CeB_6, which is a well studied material having the same crystal structure as SmB_6. Our objective here is to demonstrate that NIXS is indeed able to determine unambiguously and correctly the local ground state wave function in a cubic system. Finally, we present the NIXS results on SmB_6, which carries also the complication of having an intermediate valence state. We will show the consequences of our findings, not only for the experimental search for the properties of the topological surface states but, above all, for the theoretical modeling of this complex strongly correlated system.

2 Non-resonant inelastic scattering (NIXS)

The theoretical description of inelastic x-ray scattering can be found in a number of publications, see e.g. [19–27]. The double differential cross-section is the product of the Thomson photon cross section $\left(\frac{d\sigma}{d\Omega}\right)_{Tho}$ and the dynamical structure factor $S(\vec{q},\omega)$

$$\frac{d^2\sigma}{d\Omega d\omega} = \left(\frac{d\sigma}{d\Omega}\right)_{Tho} S(\vec{q},\omega)\,. \tag{1}$$

The dynamical structure factor is a function of the scattering vector $\vec{q} = \vec{k_i} - \vec{k_f}$ and the energy loss $\omega = \omega_i - \omega_f$

$$S(\vec{q},\omega) = \sum_f \left|\langle f|e^{i\vec{q}\cdot\vec{r}}|i\rangle\right|^2 \delta(\hbar\omega_i - \hbar\omega_f - \hbar\omega). \tag{2}$$

Here i and f are the initial and final states. The transition operator $e^{i\vec{q}\cdot\vec{r}}$ can be expanded in semi-normalized (Racah's normalization) spherical harmonics $C^{\hat{q}^*}_{km}$ and $C^{\hat{r}}_{km}$. This results in a sum over spherical Bessel functions $j_k(\vec{q}\cdot\vec{r})$ and the wave functions can be factorized into a radial and angular part so that $S(\vec{q},\omega)$ can be written as

$$S(\vec{q},\omega)=\sum_f \left|\sum_k^{\infty} i^k(2k+1)\langle R_f|j_k(\vec{q}\cdot\vec{r})|R_i\rangle \sum_{m=-k}^{k}\left\langle \phi_f|C^{\hat{q}^*}_{km}C^{\hat{r}}_{km}|\phi_i\right\rangle\right|^2 \times\delta(\hbar\omega_i-\hbar\omega_f-\hbar\omega). \tag{3}$$

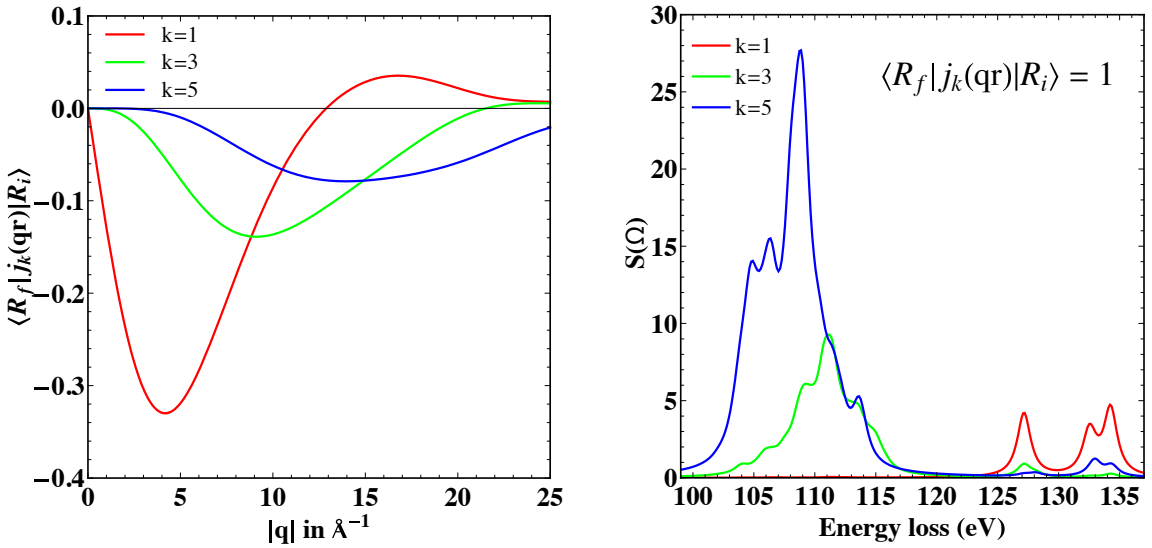

Fig. 1: *Left: k^{th} order term of the radial part of $S(\vec{q},\omega)$ for a Ce $4f^1$ ion as a function of momentum transfer. Right: k^{th} order contribution of the angular part of the scattering function expressed in terms of $S(\omega)$ versus energy transfer for $\langle R_f|j_k(\vec{q}\cdot\vec{r})|R_i\rangle$ = 1, see Eq.* (3).

Let us consider the $4d \rightarrow 4f$ ($N_{4,5}$) core-level transitions for rare-earth ions. Due to the triangle condition and parity selection rules, only terms with k=1(dipole), 3(octupole), and 5(triakontadipole) contribute. The radial part $\langle R_f|j_k(\vec{q}\cdot\vec{r})|R_i\rangle$ of the wave functions have been calculated for a Ce $4f^1$ ion within the Hartree-Fock approximation using Cowan's code [28] and the kth contributions are shown as function of momentum transfer $|\mathbf{q}|$ in the left panel of Fig. 1. For moderate magnitudes of $|\vec{q}|$ the radial part is dominated by dipole scattering, but already at 5 Å^{-1} octopole scattering is non-negligible, and at even higher momentum transfers the scattering is dominated by the higher multipoles. This behavior is commonly called q-dependent multipole selection rules. The right panel of Fig. 1 shows the kth order of the angular part as function of energy loss. Higher multipoles have different selection rules so that extra intensity at different energy losses becomes visible in the angular part, when at large $|\vec{q}|$ octupole and triakontadipole transitions take place.

Having described the $|\vec{q}|$ dependence of the NIXS intensities, we now focus on the vector $\hat{q}$ dependence which is at the heart of our study. We first of all show the sensitivity of NIXS at the $N_{4,5}$ edge to anisotropies in the wave function in general, by comparing simulated spectra for different directions of $\hat{q}$. These anisotropies arise, for example, when the initial and final states in Eq. (3) are eigenstates of a Hamiltonian that contains in addition to the atomic Coulomb and spin-orbit interactions also crystal-field terms.

We note that the interference terms which vanish if the angular intensity is integrated over all directions $\hat{q}$ [25, 26] are included in our calculations. Figure 2 shows the simulation of $S(\vec{q},\omega)$ for large momentum transfers for the three pure J_z states of a $J = 5/2$ ion like Ce^{3+} with one f electron (f^1 configuration). Some realistic broadening due to life time and instrumental resolution has been considered (see below). Here [001] is the quantization axis. The pure states have rotational symmetry perpendicular to the quantization axis so that we compare so-called in-plane scattering ($\hat{q}\|[100]$) with scattering out-of-plane, i.e., for $\hat{q}\|[001]$ and some direction

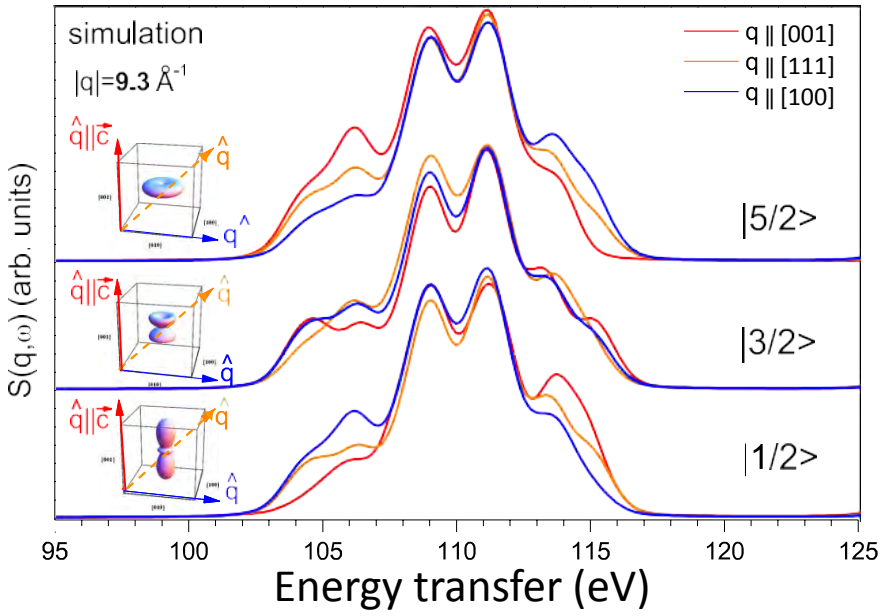

Fig. 2: *Simulations for a Ce $4f^1$ ion: Comparison of the in-plane and out-of-plane scattering function $S(\vec{q},\omega)$ of pure J_z states, in-plane $\hat{q}\|[100]$ (blue), out-of-plane $\hat{q}\|[001]$ (red), and in between $\hat{q}\|[101]$ (orange). The calculations are for $|\vec{q}|$ =9.3 Å^{-1} and are convoluted with a Lorentzian with FWHM=0.3 eV and a Gaussian with FWHM=1.32 eV. Adapted from Ref. [27]*

in between ($\hat{q}\|[111]$). There is a clear directional dependence, so that the different J_z states are distinguishable. This is at first sight similar or analogous to the in-plane/out-of-plane polarization dependence in soft x-ray absorption at the cerium $M_{4,5}$ edge ($3d \rightarrow 4f$) [18, 29]. However, on a closer look one can observe that the spectrum for ($\hat{q}\|[111]$) can not be expressed as a linear combination of the $\hat{q}\|[100]$ and $\hat{q}\|[001]$ spectra. This shows that the directional dependence in NIXS contains more information than the polarization dependence in XAS.

A nice demonstration that NIXS provides more information than XAS is given by the study by Willers *et al.* [27]. Let us consider a Ce $4f^1$ ion in a tetragonal crystal field. The sixfold degenerate Hund's rule ground state of Ce^{3+}(J = 5/2) is split into three Kramer's doublets and the eigenfunctions can be represented in the basis of $|J_z\rangle$ when the fourfold symmetric tetragonal [001] axis is chosen as quantization axis. There are two Γ_7 doublets $\Gamma_7^1 = \alpha|\pm 5/2\rangle + \sqrt{1-\alpha^2}|\mp 3/2\rangle$ and $\Gamma_7^2 = \sqrt{1-\alpha^2}|\pm 5/2\rangle - \alpha|\mp 3/2\rangle$, and one Γ_6 which is a pure $|\pm 1/2\rangle$ doublet. The Γ_6 as a pure $|\pm 1/2\rangle$ has full rotational symmetry around [001] but the mixed Γ_7 states do not. Both Γ_7 states have a fourfold symmetry around [001] and for a given spatial distribution of the two Γ_7 states there are two solutions which differ in their orientations within the (001) plane by 45°. Which orientation applies to the ground state depends on the sign of α. For $\alpha > 0$ the wings of a Γ_7 ground state point along [100] and for $\alpha < 0$ along [110]. The situation for $\alpha = -0.68 < 0$ is depicted in Fig. 3, together with the corresponding NIXS spectra calculated for $\hat{q}\|[100]$ and $\hat{q}\|[110]$. It clearly shows that the two spectra are distinguishable and a NIXS experiment (see Ref. [27]) has proven the feasibility. In XAS the situation is very different. The signal in XAS is purely dipole and can therefore not give any insight into the orientation of these fourfold rotational invariant orbitals; the spectra look identical for any polarization perpendicular to the c-axis.

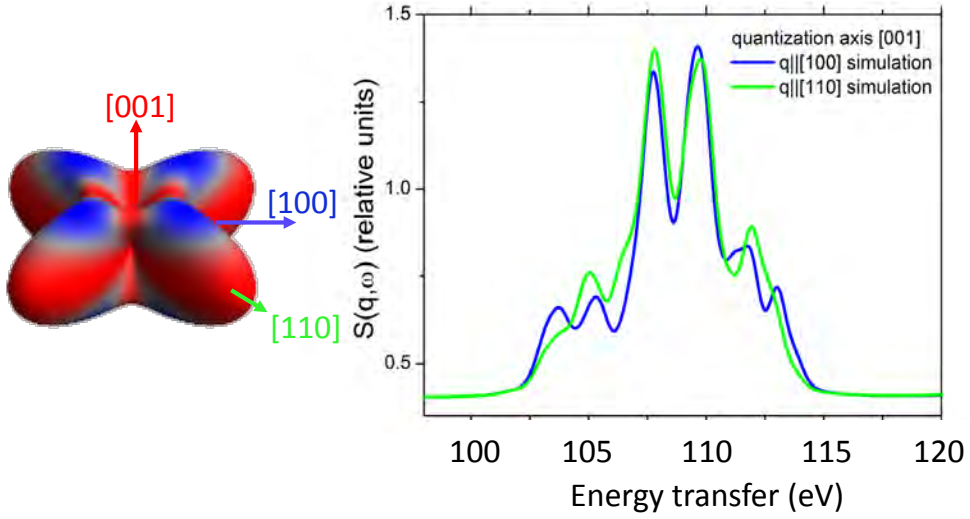

Fig. 3: *Simulation (top): The scattering function $S(\vec{q},\omega)$ for two in-plane directions $\hat{q}\|[100]$ (blue) and $\hat{q}\|[110]$ (green) assuming a $\Gamma_7^1 = \alpha|\pm 5/2\rangle + \sqrt{1-\alpha^2}|\mp 3/2\rangle$ ground state for a Ce $4f^1$ ion in a tetragonal crystal field with $\alpha < 0$. The calculations are convoluted with a Lorentzian with FWHM=0.3 eV and a Gaussian with FWHM=0.7 eV.*

We note that for a 45° rotation around the c-axis [001], i.e., for a positive value of α, the NIXS spectra are inverted. We found that these in-plane NIXS spectra are fairly insensitive to the precise value of α as long as α is neither zero nor one. In the latter case the orbital would have full rotational symmetry around [001] and consequently $S(\vec{q},\omega)$ would look the same for both in-plane directions.
To conclude this section, NIXS is a spectroscopic method that can determine the active local orbital wave function with great detail due to the fact that higher than dipole transitions are utilized if the measurement is carried out with high momentum transfers.

3 The local ground state wavefunction of CeB_6

The material class of rare earth hexaborides has attracted considerable attention over the years. It comprises of a variety of different fascinating ground states (see Ref. [30] and references therein) which include exotic magnetically ordered phases, heavy fermion behavior, as well as Kondo insulating ground states. CeB_6 is an important member of this material class and has been intensively studied for its rich magnetic phase diagram [31]. It crystallizes in the cubic CsCl structure. Fig. 4 displays how the crystal-electric field splits the sixfold degenerate $j = 5/2$ multiplet state of the Ce $4f^1$ into a Γ_8 quartet and Γ_7 doublet.
Upon cooling CeB_6 enters a hidden-order phase at 3.2 K followed by an antiferromagnetic phase below 2.4 K. The application of an external field induces a dipole component with the wave vector of the quadrupolar ordering [33]. Theory suggests that the multipolar moments of the localized $4f$ electrons interact with each other via the itinerant $5d$ conduction electrons, breaking up the fourfold ground-state degeneracy of the Ce $4f$ wave function in the cubic crystal field stabilizing an antiferro-quadrupolar (AFQ) order [34, 35], a conjecture that by now

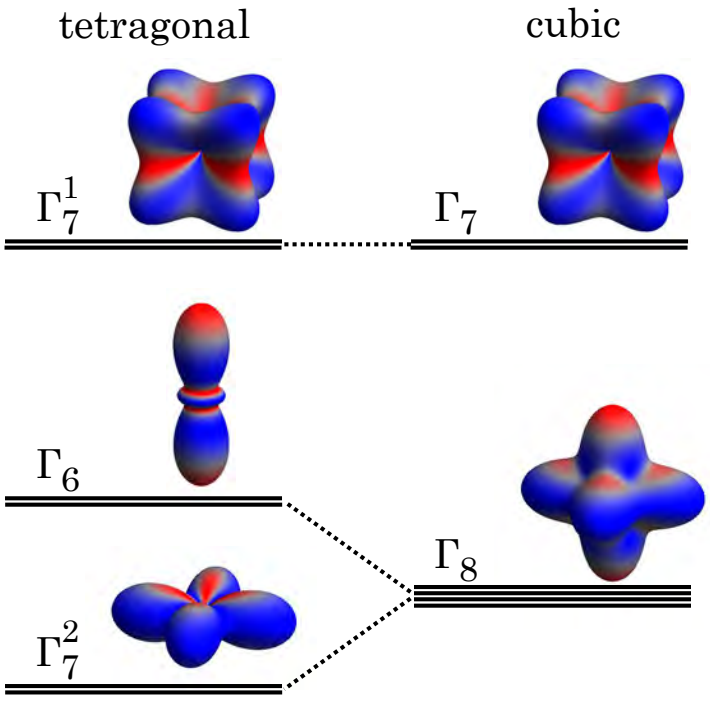

Fig. 4: *Electron density plots for an f-electron in Ce^{3+}, left for tetragonal and right for cubic point symmetry. For tetragonal symmetry the crystal-field states expressed in J_z representation are $\Gamma_6 = |\pm 1/2\rangle$, $\Gamma_7^1 = \alpha|\pm 5/2\rangle - \sqrt{1-\alpha^2}|\mp 3/2\rangle$ and $\Gamma_7^2 = \sqrt{1-\alpha^2}|\pm 5/2\rangle + \alpha|\mp 3/2\rangle$ with $\alpha^2 \leq 1$; for cubic symmetry $\alpha = \sqrt{1/6}$ so that $\Gamma_7^1 = \sqrt{1/6}|\pm 5/2\rangle - \sqrt{5/6}|\mp 3/2\rangle$ and $\Gamma_8 = (|\pm 1/2\rangle; \sqrt{5/6}|\pm 5/2\rangle + \sqrt{1/6}|\mp 3/2\rangle)$. Figure adapted from Ref. [32]*

has received credibility from studies using resonant x-ray diffraction [36, 37], inelastic neutron scattering [38–40], and electron spectroscopy [41, 42].

The quartet ground state had been originally deduced from an unusual low temperature shift of the crystal-field excitation at 46 meV in Raman and inelastic neutron scattering data [43, 44]. The energy shift was interpreted as a splitting of the quartet ground state in the low temperature phase in accordance with electron paramagnetic resonance (EPR) measurements [45]. A quartet ground state is also consistent with findings of the magnetic anisotropy [46], magnetic neutron form factor measurements [47], as well as x-ray diffraction (XRD) measurements of the electron density distribution at low temperatures and 300 K [48] with the claim that a level inversion may occur at higher temperatures [49].

Our objective now is to apply NIXS on this cubic system in the paramagnetic phase using the Ce $N_{4,5}$ ($4d \rightarrow 4f$) excitation and to verify that the local ground state wave function is indeed the quartet Γ_8.

The NIXS measurements were performed at the beamline P01 of PETRA-III. The incident energy was selected with a Si(311) double monochromator. The P01 NIXS end-station has a vertical geometry with twelve Si(660) 1 m radius spherically bent crystal analyzers that are arranged in 3×4 array (see Fig. 5). The fixed final energy was 9690 eV. The analyzers were positioned at scattering angles of $2\,\theta \approx 150°$, 155°, and 160° which corresponds at elastic scattering

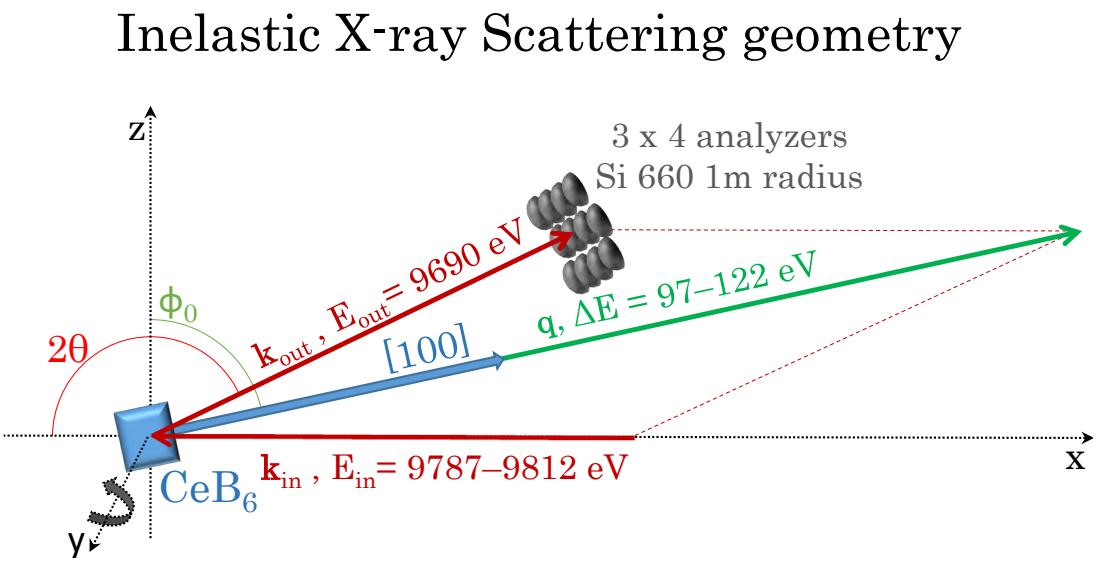

Fig. 5: *Scattering geometry of the NIXS experiment for a typical $N_{4,5}$ edge scan with $\hat{q} \parallel [100]$. Figure adapted from Ref. [32].*

to an averaged momentum transfer of $|\vec{q}| = (9.6 \pm 0.1)\,\text{Å}^{-1}$. The scattered beam was detected by a position sensitive detector. The instrumental energy resolution was ≈ 0.7 eV. A sketch of the scattering geometry, showing the incoming and outgoing photons as well as the transferred momentum $|\vec{q}|$, is given in Fig. 5 for a scan with $\hat{q} \parallel [100]$ in specular geometry. In order to realize another crystallographic direction, e.g., $\hat{q} \parallel [110]$, the sample can be turned with respect to the scattering triangle, or a different sample with another polished surface may be mounted in specular geometry.

Figure 6 shows the NIXS spectrum across the Ce $N_{4,5}$ ($4d \rightarrow 4f$), $N_{2,3}$ ($4p \rightarrow 4f$), and N_1 ($4s \rightarrow 4f$) edges. The clear presence of the $N_{2,3}$ and N_1 edges demonstrates unambiguously that higher than dipole transition operators are active here. The accompanying Compton contribution has its maximum at about 350 eV energy transfer. It is important to note that the Ce white lines are clearly discerned from the Compton scattering, and that especially the Ce $N_{4,5}$ white lines stand out with an excellent signal to background ratio, i.e., $N_{4,5}$ NIXS is an extremely powerful spectroscopic method.

The bottom set of curves in the top panel of Fig. 7 shows the Ce $N_{4,5}$ NIXS spectra of CeB_6 (dots) taken at 17 K, for the three momentum directions $\hat{q} \parallel [100]$ (black dots), $\parallel [110]$ (green dots), and $\parallel [111]$ (red dots). The temperature of 17 K is low enough to assure that only the local ground state is populated since the excited crystal-field state is at 46 meV [43, 44]. A constant background has been subtracted to account for the (weak) Compton signal (about 12% of the signal peak) (see Fig. 6).

There is a clear directional dependence that shows up strongest in the energy interval of 103 to 106 eV. Especially the $\hat{q} \parallel [100]$ direction differs from the $\hat{q} \parallel [110]$ and [111]. We can obtain a more detailed view of the directional dependence by constructing the difference spectra $I_{\hat{q} \parallel [100]} - I_{\hat{q} \parallel [110]}$ that is displayed as dichroism in the bottom panel of Fig. 7 (black dots).

The Ce $N_{4,5}$ NIXS data are simulated by calculating the $4d^{10}4f^1 \rightarrow 4d^9 4f^2$ transition using the

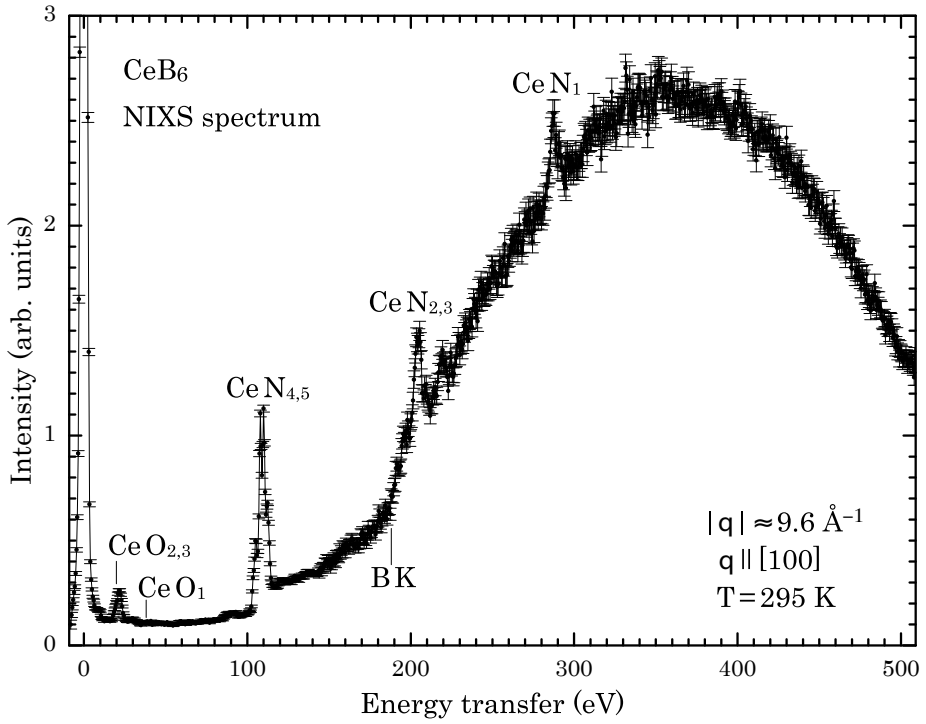

Fig. 6: *Experimental NIXS spectra of CeB_6: a wide scan covering the Ce O_5, $N_{4,5}$, $N_{2,3}$, and N_1 edges, the B K edge as well as the Compton signal. The direction of momentum transfer is $\hat{q} \parallel [100]$. Figure adapted from Ref. [32].*

full multiplet code *Quanty* [50] which includes Coulomb as well as spin-orbit interactions. A Gaussian and a Lorentzian broadening of FWHM = 0.7 eV and 0.4 eV, respectively, are used to account for the instrumental resolution and life time effects. The atomic Hartree-Fock values were adjusted via the peak positions, resulting in reductions of 30 % and 22 % for the $4f$-$4f$ and $4d$-$4f$ Coulomb interactions, respectively. The reduction accounts for configuration-interaction effects not included in the Hartree-Fock scheme [16]. A momentum transfer of $|\vec{q}| = 9.2\,\text{Å}^{-1}$ has been used for the simulations (and not the experimental value of $9.6 \pm 0.1)\,\text{Å}^{-1}$) so that the experimental peak ratio of the two main features around 108 and 110 eV is reproduced best. This fine tuning optimizes the multipole contributions to the scattering functions to mimic a minor adjustment of the calculated radial wave functions of the Ce^{3+} *atomic* wave function (see e.g. Ref. [27]).

We now compare the measured spectra and the dichroism therein with the simulations for the two possible scenarios, namely one with the Γ_7 doublet as ground state and the other with the Γ_8 quartet. The results are plotted in Fig. 7 (a). The Γ_8 quartet scenario reproduces in great detail the experimental spectra for all three $\hat{q}$ directions. In contrast, the simulation based on the Γ_7 doublet exhibits large discrepancies with respect to the experiment: the intensities of several features in the spectra are not correct. To make the difference between the two scenarios even more contrasting, we compare the experimental and calculated dichroic spectra, i.e. $\mathrm{I}_{\hat{\mathbf{q}} \parallel [100]} - \mathrm{I}_{\hat{\mathbf{q}} \parallel [110]}$, as displayed in bottom panel (b). There is an excellent match for the Γ_8 quartet ground state scenario but a large mismatch for the Γ_7 doublet. From these comparisons we can unambiguously conclude that the Γ_8 quartet forms the ground state in CeB_6.

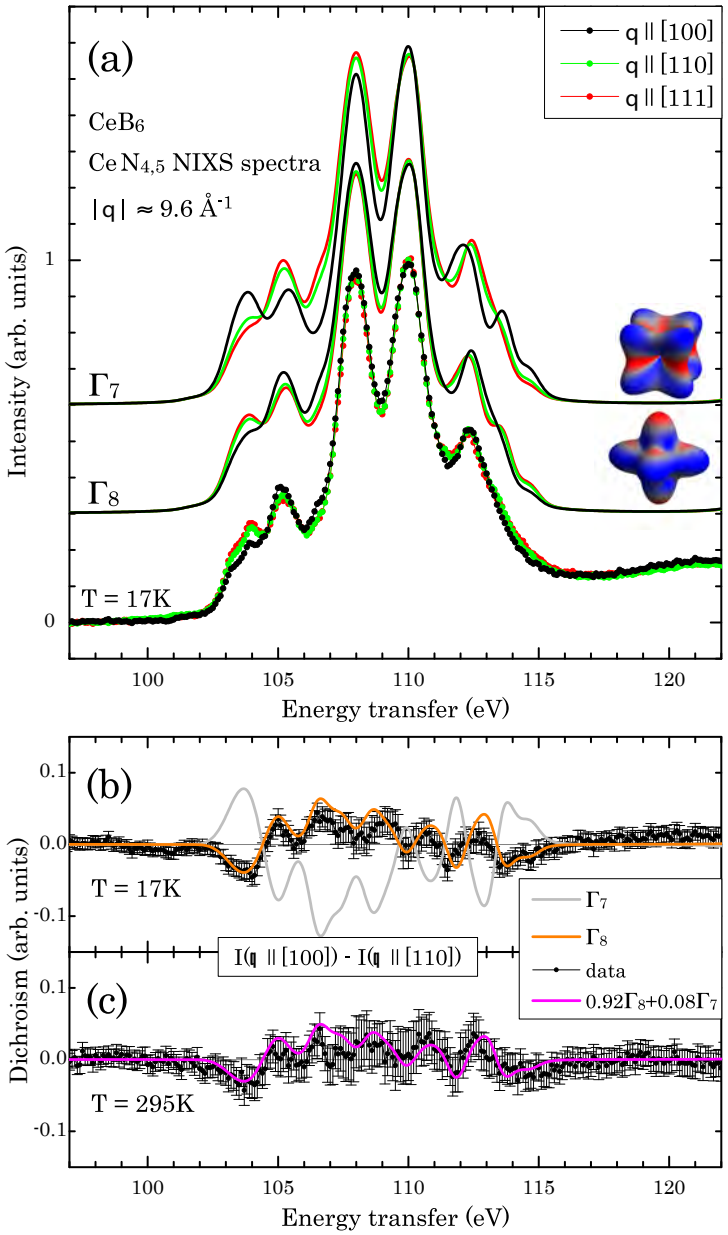

Fig. 7: *Top panel (a): calculated and experimental NIXS spectra of the Ce $N_{4,5}$-edge of CeB_6 for the three transferred momentum directions $\hat{q} \parallel [100]$, [110], and [111]. Bottom panel: difference spectra $I(\hat{q} \parallel [100]) - I(\hat{q} \parallel [110])$ (black dots) (b) at low T and (c) at room temperature and respective simulations (see text). Figure adapted from Ref. [32].*

We have also taken spectra at T = 295 K. The spectra look very similar to the low temperature data but the dichroism is reduced by about 20%, see bottom panel (c) of Fig. 7. This reduction in the dichroism is fully consistent with a partial population of the excited Γ_7 state at 46 meV. A simulation in which the Boltzmann weighted contributions of the Γ_8 and Γ_7 states are taken into account is represented by the magenta line in panel (c) of Fig. 7. The excellent agreement provides yet another evidence for the thorough understanding we have obtained using NIXS on the Ce $4f$ symmetry and crystal-electric field effects in CeB_6.

4 The local ground state wavefunction of intermediate valent SmB_6

Having established that core-level NIXS is a powerful and reliable spectroscopic method to determine the local ground state wavefunction for CeB_6, we are now ready to tackle the puzzle of SmB_6. The intermediate valent and Kondo insulator SmB_6 [51–55] has attracted considerable attention recently due to the prediction that this system should be a topological insulator [56–61]. If true, SmB_6 would be the material to qualify as the first strongly correlated topological insulator. Indeed, the robust metallicity which is attributed to a topologically protected surface state could be a promising explanation for the long-standing mysterious low-temperature residual conductivity of SmB_6 [53, 54, 62]. Many experimental techniques like angle-resolved photoelectron spectroscopy (ARPES) [63–71], scanning tunneling spectroscopy [72–76], resistivity and surface conductance measurements [77–84] have been applied to unveil its topological properties. A review is given by Ref. [85, 86].

In SmB_6, the strong hybridization of the low lying $4f$ states with conduction band d states gives rise to a hybridization gap of the order of 20 meV [63–68] and also leads to a partial occupation of the $4f$ shell or a mixture of the Sm f^6 (2+) and f^5 (3+) configurations. For the valence at low temperatures, values of around 2.6 have been determined experimentally [87–93]. Hence the local electronic structure is described by the Hund's rule ground states of the Sm f^6 (2+) and f^5 (3+) configurations with total orbital momenta of $J = 0$ and $5/2$, respectively. The $J = 5/2$ multiplet is further split into a Γ_7 doublet and a Γ_8 quartet due to the cubic crystal-electric field (CEF). Fig. 8 shows the ground- and first excited state of the two Sm configurations plus their electron charge density distributions. The charge densities of the $J = 0$ and 1 states are spherical since neither the $J = 0$ or 1 are split in a cubic potential [95]. This is contrasted by the charge densities of the CEF-split J = 5/2 multiplet (and J = 7/2, not shown) that are anisotropic. The CEF scheme of SmB_6 is however, not established. The classical tool, inelastic neutron scattering, has not been able to identify the CEF states, possibly due to the superposition of both Sm f^5 and f^6 configurations in this mixed valent compound and the strong neutron absorption despite double isotope samples [10,11,96]. A sharp excitation at 14 meV close to the hybridization gap was reported. It was assigned to a spin exciton and not to a CEF excitation since its intensity does not follow the $4f$ magnetic form factor. Further magnetic intensities at about 35 meV, 115 meV, and 85 meV have been assigned to the inter-multiplet transitions of the Sm^{2+} configuration and of the CEF split Sm^{3+} configuration (see Fig. 8), and to some magnetoelastic coupling, respectively. In-gap transitions at about 15 meV in Raman spectra could be interpreted as CEF excitations but Raman does not yield the information about which state forms the ground state [97, 98]. A semi-empirical extrapolation method can predict CEF parameters across the rare earth series for highly diluted systems [99]. Applying such an extrapolation to the measured CEF schemes of REB_6 with RE = Ce, Pr, and Nd [43, 100] yields for SmB_6 a CEF splitting of the order of 15 meV with the Γ_8 quartet as the ground state. However, the Kondo insulator SmB_6 is not a highly diluted system and it is definitely not an ionic system but highly intermediate valent instead, questioning the validity of such an extrapolation.

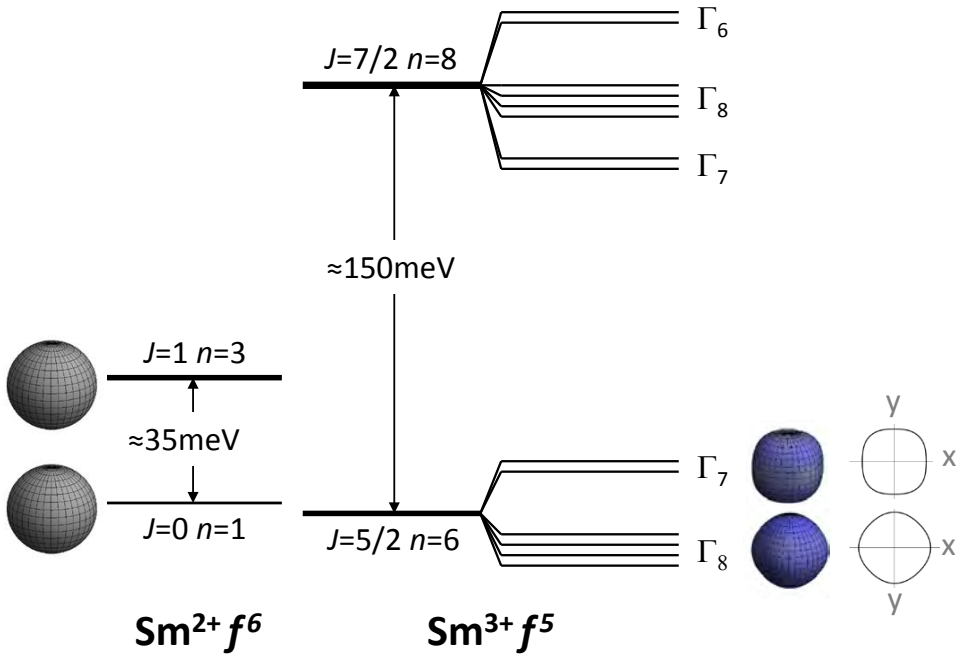

Fig. 8: *Sm^{2+} and Sm^{3+} total energy level diagram. The Sm^{2+} configuration is split into a J=0 and J=1, and the Sm^{3+} into a J=5/2 and J=7/2 multiplet. The label n indicates the degeneracy. The Sm^{3+} multiplets are further split (Γ_i) by the cubic crystal-electric field. The insets show the corresponding charge densities for six and five electrons and their 2D projections, respectively. Figure adapted from Ref. [94].*

We have carried out $N_{4,5}$ NIXS experiments on SmB_6 and also on Sm_2O_3, and Eu_2O_3 which we used as $4f^5$ and $4f^6$ reference systems, respectively. Fig. 9 shows the spectra: SmB_6 (blue dots), Sm_2O_3 (purple dots) and Eu_2O_3 (dark yellow dots) after subtraction of a linear background and scaling to the Compton background. We have artificially shifted the Eu_2O_3 spectrum by 6.8 eV to lower energies in order to account for the higher atomic number. We also have multiplied the Sm_2O_3 spectrum by a factor 0.6 and the Eu_2O_3 one by 0.4. We have done this in order to investigate whether the SmB_6 spectrum can be interpreted using those of Sm_2O_3 and Eu_2O_3. We thus compare the weighted sum of Sm_2O_3 and Eu_2O_2 (see dark cyan line) with the SmB_6 spectrum, and we can observe that the weighted sum spectrum provides a satisfactory reproduction. This means that our NIXS data indicates that the Sm valence is about 2.6, in good agreement with other studies using a variety of different experimental methods [87–93].

Fig. 9 (b) shows the $N_{4,5}$ full multiplet simulation for the Sm^{3+} (purple line) and Sm^{2+} (dark yellow line). The weighted sum (60% and 40%) of the simulated curves (dark cyan) describes the SmB_6 spectrum very well in the energy region between 120 and 135 eV. This is the region where the high multipole scattering dominates. In the region above $\approx$ 135 eV, where the spectrum is given mostly by the dipole transitions the simulation produces spectral features that are too sharp with respect to the experiment because the interference with the continuum states is not included in the calculations. The high multipole excitations are more realistically reproduced since they are lower in energy and therefore further away from the continuum states and consequently more excitonic [101].

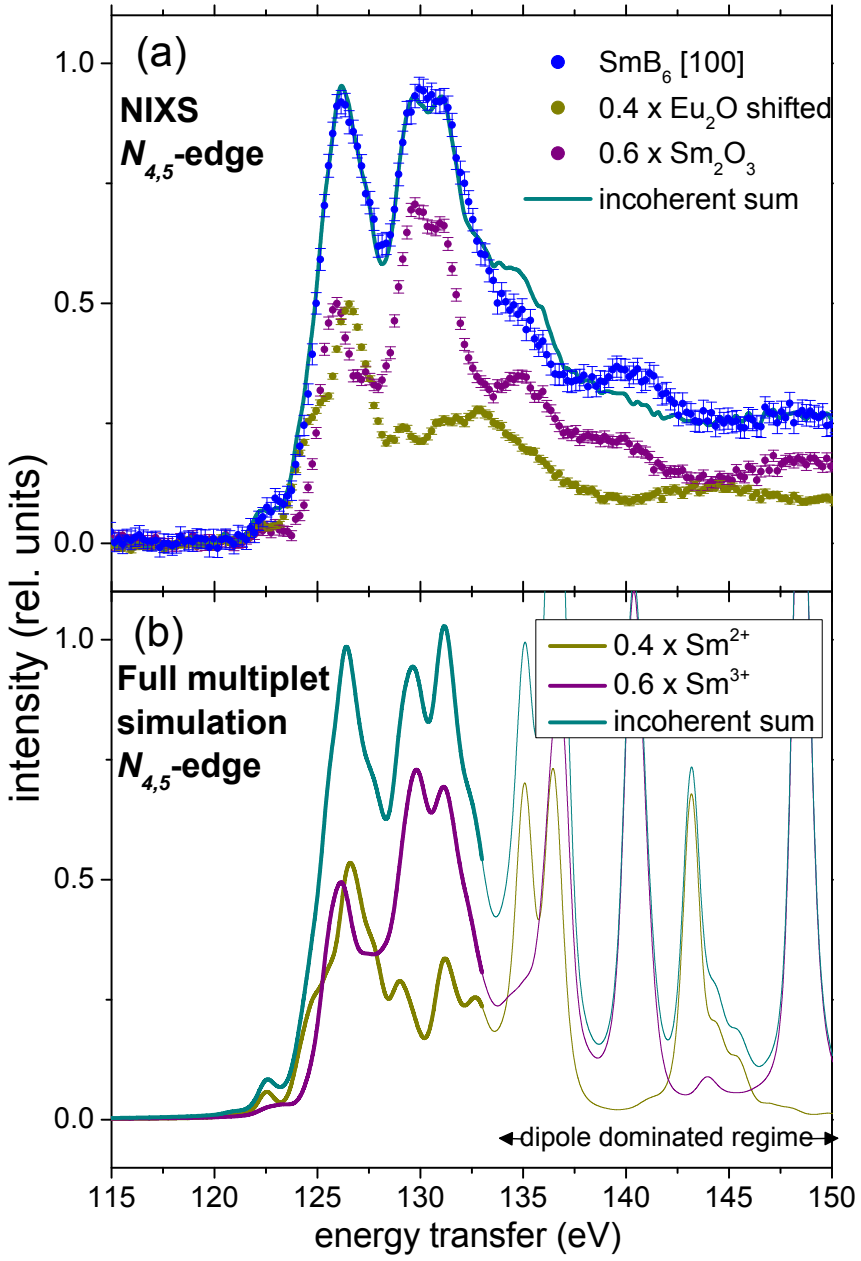

Fig. 9: *(a) Experimental SmB_6 data for $\hat{q}\|[100]$ (blue dots) together with the weighted sum (dark cyan line) of the experimental Sm_2O_3 (f^5) (purple dots) and energy-shifted experimental Eu_2O_3 (f^6) (dark yellow dots). (b) Full multiplet simulation of Sm^{3+} (purple line) and Sm^{2+} spectra (dark yellow line) and their weighted sum (dark cyan). Figure adapted from Ref. [94].*

Figure 10 shows the directional dependence of the Sm $N_{4,5}$ of SmB_6. Although the effect is small, there are clear differences between the spectra in the energy regions marked with red arrows. At about 126 eV energy transfer the scattering of the $\hat{q}\|[110]$ (light green dots) and $\hat{q}\|[111]$ (dark green dots) directions are both stronger than for the $\hat{q}\|[100]$ (blue dots), and at about 140 eV it is opposite. To show these directional differences in a more transparent manner, we also present in Fig. 10 the difference spectrum between the $\hat{q}\|[100]$ and $\hat{q}\|[111]$ (black dots): this so-called dichroic spectrum has unambiguously a negative peak at 126 eV whereas it displays positive intensity in a broader region around 140 eV.

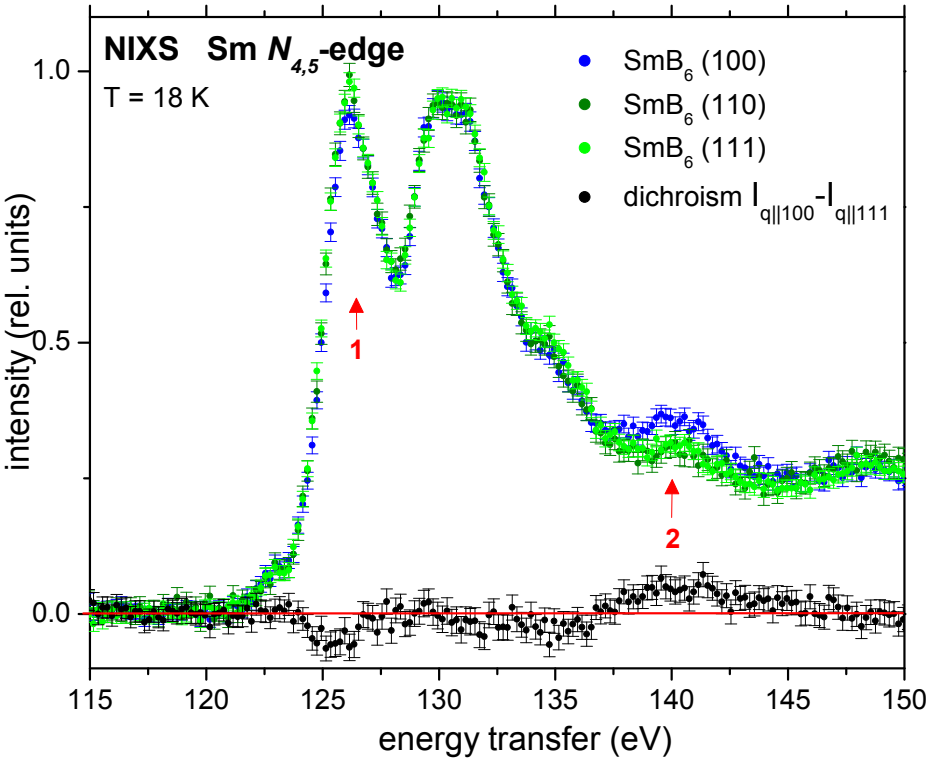

Fig. 10: *SmB_6 NIXS data at 16 K for $\hat{q}||[100]$ (blue dots), $\hat{q}||[110]$ (dark green dots), and $\hat{q}||[111]$ (light green dots). The difference spectrum between the $\hat{q}||[100]$ and $\hat{q}||[111]$ directions is also displayed (black dots). Figure adapted from Ref. [94].*

To interpret the observed directional dependence, it is important to know how each CEF state or multiplet component contributes to the dichroic signal. Therefore, $S(\vec{q},\omega)$ has been calculated taking into account a cubic CEF for the Sm^{3+} f^5 ground state multiplet with $J=5/2$ assuming a Γ_8 quartet or a Γ_7 doublet ground state, and for the Sm^{2+} f^6 multiplets with $J=0$ or $J=1$ (see Fig. 8). The calculations were performed for the two directions $\hat{q}||[100]$ and $\hat{q}||[111]$ and in Fig. 11 (a) the resulting dichroic signals are plotted. Here only the multipole scattering contributes to the dichroism, the dipole does not because the Sm site symmetry is cubic.

The first important finding is that the Sm^{2+} configuration does not show any dichroism at all (see dark red and green lines at zero dichroism) as we would expect for states with spherical charge densities, see Fig. 8. Hence, the observed directional dependence of the signal is solely due to the initial state of the Sm^{3+} Hund's rule ground state. The second important finding is that the Γ_8 and Γ_7 CEF states exhibit different and opposite dichroism (see orange and light blue lines), consistent with their opposite anisotropy in the charge densities, see Fig. 8. The opposite dichroism at 125 and 140 eV reduces the experimental challenge to a simple yes/no experiment and makes the determination of the CEF ground state of Sm^{3+} in SmB_6 straightforward.

Figure 11 (b) shows the experimental dichroic spectrum (black dots) together with the calculated ones. The two possible CEF states of the $J=5/2$ configuration have now been scaled down to 60% to quantitatively account for the Sm^{3+} component in intermediate valent SmB_6. We can clearly observe that in the regions of pronounced dichroism (see red arrows) the sign of

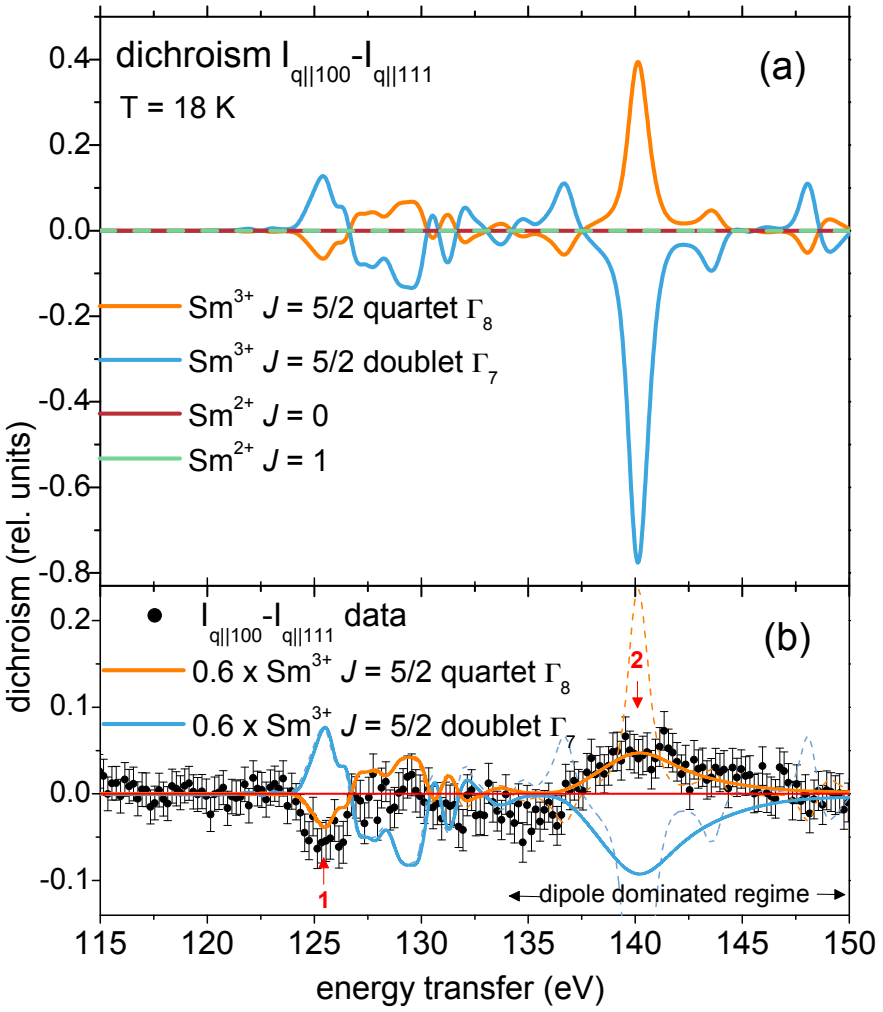

Fig. 11: *(a) simulation of the $\hat{q}$||[100] vs. $\hat{q}$||[111] dichroic spectrum for the J=0 (brown) and J=1 (green) multiplet states of the Sm^{2+} configuration as well as for the Γ_8 quartet (orange) and Γ_7 doublet (light blue) of the J=5/2 Sm^{3+} configuration; (b) experimental dichroic spectrum (black dots) and simulated dichroic spectra for the Γ_8 quartet (orange) and Γ_7 doublet (light blue) scaled with the factor of 0.6 to account for the Sm^{3+} component of the ground state; dashed lines with energy independent broadening, solid lines with extra broadening in the dipole region (see text). Figure adapted from Ref. [94].*

the experimental dichroic signal is correctly explained by the Γ_8 quartet (orange line) but not at all by the Γ_7 doublet state (light blue line). In addition, the Γ_8 reproduces the experimental dichroism quantitatively in the high multipole region (see red arrow 1). The dichroism also fits quantitatively in the dipole region (see red arrow 2) when an extra broadening is applied (FWHM $\geq$ 4 eV beyond $\approx$135 eV energy transfer) to mimic the interference with continuum states. Note that sum rules still apply, i.e., the interference with the continuum states does not change the polarization, it only affects the broadening. The dashed lines correspond to the dipole calculation without the extra broadening. These results unambiguously establish that the CEF ground state of the Sm f^5 component in SmB_6 is the Γ_8 quartet.

5 Discussion and concluding remarks

The finding that the Γ_8 quartet forms the ground state of the Sm f^5 component in SmB_6 has several consequences:

First of all, the theoretical predictions for the spin texture of the sought-after topological surface states depend very much whether the ground state of the f^5 $J = 5/2$ configuration is the Γ_8 quartet or the Γ_7 doublet CEF state [102–104]. In fact, the winding of the spin textures is opposite for the two scenarios. Our finding of the Γ_8 quartet supports very much the results of spin resolved APRES [69]. Xu *et al.* find spin polarized surface states, fulfilling time reversal as well as crystal symmetry, that have spins locked to the crystal momenta k such that at opposite momenta the surface states have opposite spins. The anticlockwise spin texture is in agreement with spin expectation values calculated by Baruselli and Vojta for a Γ_8 ground state [102, 104].

Second, details of the character of the Sm $4f$ bands matter for the formation of the hybridization gap [56–61]. Using *ab-initio* band structure calculations [105, 106, 59, 107] as a starting point, the intermediate valence of the Sm is associated with the fact that the Sm $4f_{5/2}$ bands are fully below the Fermi level for all k-points of the Brillouin zone except in the vicinity of the X-point. There the strongly dispersing Sm $5d$ band is positioned below the Fermi level; otherwise, i.e., at other k points, the Sm $5d$ is unoccupied. The symmetry of the Sm $5d$ band that is below the Fermi level at the X-point carries the label X_7^+. The Sm $4f_{5/2}$ states splits into three bands at the X-point, and have the symmetry labels X_7^-, X_7^-, and X_6^-. One of the X_7^- bands is made of the local Γ_7 wave function, while the other X_7^- band and the X_6^- band originate from the local Γ_8 wave function. See for example Kang *et al.* [107].

In order to have an insulating state, the highest and thus unoccupied $4f_{5/2}$ band must be a X_7^- as to ensure a non-crossing situation between the X_7^- band of the $4f_{5/2}$ and the X_7^+ band of the $5d$ in the region around the X-point due to hybridization. If the highest and unoccupied $4f_{5/2}$ band were a X_6^-, then there were no hybridization with the X_7^+ band of the $5d$ in the region around the X-point, with the result that the two bands cross and no gap is opened. This means that a local Γ_7 ground state would guarantee the formation of a gap, while a Γ_8 may or may not open a gap. Further material specific details then determine whether the highest band is X_7^- or X_6^-. So our finding of the Γ_8 as the local ground state wave function does not explain why SmB_6 is insulating. Reversely, knowing that SmB_6 is an insulator, our results then fix the energy order of the bands at the X-point: the highest (and unoccupied) is the X_7^- from the Γ_8, followed by the X_6^- from Γ_8, and the lowest is the X_7^- from the Γ_7.

Third, our finding of a Γ_8 local ground-state symmetry contradicts in fact the outcome of several density functional band structure calculations [105, 106, 59, 107]. In band theory, the search for the ground state symmetry in SmB_6 translates into the question in which band the hole in the $J = 5/2$ manifold resides. Kang *et al.* reported for the X-point an unoccupied $4f$ X_7^- state of Γ_7 origin [107]. Also their k-integrated $4f$ $J = 5/2$ partial density of states (pDOS) shows the hole residing in the Γ_7 band, in line with the fact that the center of gravity of the Γ_7 pDOS is higher in energy than that of the Γ_8. We would like to note that many theoretical studies have quoted these band structure calculations for having produced a local Γ_8 ground state! This is

incorrect. Perhaps the mistake has been made by looking at the Γ-point: there the Γ_7^- band is indeed lower than the Γ_8^- band which is closer to the Fermi level giving rise to the wrong expectation that the *local* Γ_8 is the state with the hole. However, we would like to point out that looking at just one particular point in the Brillouin zone is not sufficient for extracting the local crystal field scheme. It can only be deduced from the integration over the entire Brillouin zone. In fact, realizing that crystal-field effects are determined mainly by hybridization, the Γ-point is perhaps the worst possible location in k-space to look at since there the $4f$ and the $5d$ are non-bonding due to opposite parity, a virtue that is the very starting point for proposing SmB_6 to be topologically non-trivial.

Fourth, we would like to note that the experimentally observed dichroism in our NIXS spectra can be explained by a pure Γ_8 state, weighted with 0.6 to account for the contribution of the $4f^5$ configuration in the ground state of SmB_6, see Fig. 11. This is surprising in view of the intermediate valent state of the compound, and in view that bands are important for the much discussed low energy properties. A conclusion that could be drawn from this is that the $4f$ bands may be extremely narrow, much narrower than the crystal-field splitting between the Γ_8 and Γ_7 states. The fact that the spectral responses of $4f$ ions are dominated by multiplet structures suggests that the hopping integral for the transfer of a electron from a $4f^6$ to a neighboring $4f^5$ site will be hampered by the fact that the ground state of a $4f^6$ ion is a $J = 0$ state and that of a $4f^5$ ion a $J = 5/2$. It is not impossible to convert a $4f^6$ $J = 0$ to a $4f^5$ $J = 5/2$ and simultaneously a $4f^5$ $J = 5/2$ to a $4f^6$ $J = 0$ by transferring only an $s = 1/2$ particle without energy cost, but the probability for such a large change in quantum numbers is tiny and is given by the *fractional parentage* as described in the recent lecture notes of Sawatzky [108].

To summarize, we have utilized the high multipole contributions in the core-level non-resonant inelastic x-ray scattering process to determine the symmetry of the Sm crystal-field ground state $4f$ wave function in SmB_6. We have found a clear directional dependence of the spectra that allows for the unambiguous identification of the Γ_8 quartet state of the Sm f^5 J=$5/2$ configuration as the state which governs the topological properties of SmB_6. Follow-up calculations should be performed within a reduced basis of only Γ_8 states for the construction of a low-energy many-body Hamiltonian.

Acknowledgments

I would like to acknowledge Andrea Severing, Martin Sundermann, Maurits Haverkort, and Peter Thalmeier for their invaluable input.

References

[1] J.-H. Park, L.H. Tjeng, A. Tanaka, J.W. Allen, C.T. Chen, P. Metcalf, J.M. Honig, F.M.F. de Groot, and G.A. Sawatzky, Phys. Rev. B **61**, 11506 (2000)

[2] T. Mizokawa, L.H. Tjeng, H.-J. Lin, C.T. Chen, S. Schuppler, S. Nakatsuji, H. Fukazawa, and Y. Maeno, Phys. Rev. B **69**, 132410 (2004)

[3] A. Tanaka, J. Phys. Soc. Jpn. **73**, 152 (2004)

[4] A.I. Poteryaev, A.I. Lichtenstein, and G. Kotliar, Phys. Rev. Lett. **93**, 086401 (2004)

[5] S. Biermann, A. Poteryaev, A.I. Lichtenstein, and A. Georges, Phys. Rev. Lett. **94**, 026404 (2005)

[6] M.W. Haverkort, Z. Hu, A. Tanaka, W. Reichelt, S.V. Streltsov, M.A. Korotin, V.I. Anisimov, H.H. Hsieh, H.-J. Lin, C.T. Chen, D.I. Khomskii, and L.H. Tjeng, Phys. Rev. Lett. **95**, 196404 (2005)

[7] T.C. Koethe, Z. Hu, M.W. Haverkort, C. Schüßler-Langeheine, F. Venturini, N.B. Brookes, O. Tjernberg, W. Reichelt, H.H. Hsieh, H.-J. Lin, C.T. Chen, and L.H. Tjeng, Phys. Rev. Lett. **97**, 116402 (2006)

[8] C.F. Chang, T.C. Koethe, Z. Hu, J. Weinen, S. Agrestini, L. Zhao, J. Gegner, H. Ott, G. Panaccione, H. Wu, M.W. Haverkort, H. Roth, A.C. Komarek, F. Offi, G. Monaco, Y.-F. Liao, K.-D. Tsuei, H.-J. Lin, C.T. Chen, A. Tanaka, and L.H. Tjeng, Phys. Rev. X **8**, 021004 (2018)

[9] A. Severing, E. Holland-Moritz, B.D. Rainford, S.R. Culverhouse, and B. Frick, Phys. Rev. B **39**, 2557 (1989)

[10] P.A. Alekseev, V.N. Lazukov, R. Osborn, B.D. Rainford, I.P. Sadikov, E.S. Konovalova, and Y.B. Paderno, Europhys. Lett. **23**, 347 (1993)

[11] P.A. Alekseev, J.M. Mignot, J. Rossat-Mignod, V.N. Lazukov, I.P. Sadikov, E.S. Konovalova, and Y.B. Paderno, J. Phys.: Condens. Matter **7**, 289 (1995)

[12] D.T. Adroja, K. McEwen, J.-G. Park, A.D. Hillier, N. Takeda, P. Riseborough, and T. Takabatake, J. Optoelectron. Adv. M. **10**, 1719 (2008)

[13] D.T. Adroja, A.D. Hillier, Y. Muro, T. Takabatake, A.M. Strydom, A. Bhattacharyya, A. Daoud-Aladin, and J.W. Taylor, Phys. Scr. **88**, 068505 (2013)

[14] C.T. Chen, L.H. Tjeng, J. Kwo, H.L. Kao, P. Rudolf, F. Sette, and R.M. Fleming, Phys. Rev. Lett. **68**, 2543 (1992)

[15] F. de Groot, J. Electron. Spectrosc. Relat. Phenom. **67**, 529 (1994)

[16] A. Tanaka and T. Jo, J. Phys. Soc. Jpn. **63**, 2788 (1994)

[17] S.I. Csiszar, M.W. Haverkort, Z. Hu, A. Tanaka, H.H. Hsieh, H.-J. Lin, C.T. Chen, T. Hibma, and L.H. Tjeng, Phys. Rev. Lett. **95**, 187205 (2005)

[18] P. Hansmann, A. Severing, Z. Hu, M.W. Haverkort, C.F. Chang, S. Klein, A. Tanaka, H.H. Hsieh, H.-J. Lin, C.T. Chen, B. Fåk, P. Lejay, and L.H. Tjeng, Phys. Rev. Lett. **100**, 066405 (2008)

[19] W. Schülke: *Electron Dynamics by Inelastic X-Ray Scattering* (Oxford University Press, 2007)

[20] J.A. Soininen, A.L. Ankudinov, and J.J. Rehr, Phys. Rev. B **72**, 045136 (2005)

[21] M.W. Haverkort, A. Tanaka, L.H. Tjeng, and G.A. Sawatzky, Phys. Rev. Lett. **99**, 257401 (2007)

[22] R.A. Gordon, G.T. Seidler, T.T. Fister, M.W. Haverkort, G.A. Sawatzky, A. Tanaka, and T.K. Sham, Europhys. Lett. **81**, 26004 (2008)

[23] R. Caciuffo, G. van der Laan, L. Simonelli, T. Vitova, C. Mazzoli, M.A. Denecke, and G.H. Lander, Phys. Rev. B **81**, 195104 (2010)

[24] J.A. Bradley, G.T. Seidler, G. Cooper, M. Vos, A.P. Hitchcock, A.P. Sorini, C. Schlimmer, and K.P. Nagle, Phys. Rev. Lett. **105**, 053202 (2010)

[25] J.A. Bradley, K.T. Moore, G. van der Laan, J.P. Bradley, and R.A. Gordon, Phys. Rev. B **84**, 205105 (2011)

[26] G. van der Laan, Phys. Rev. Lett. **108**, 077401 (2012)

[27] T. Willers, F. Strigari, N. Hiraoka, Y.Q. Cai, M.W. Haverkort, K.-D. Tsuei, Y.F. Liao, S. Seiro, C. Geibel, F. Steglich, L.H. Tjeng, and A. Severing, Phys. Rev. Lett. **109**, 046401 (2012)

[28] R. Cowan: *The theory of atomic structure and spectra* (University of California, Berkley, 1981)

[29] T. Willers, B. Fåk, N. Hollmann, P.O. Körner, Z. Hu, A. Tanaka, D. Schmitz, M. Enderle, G. Lapertot, L.H. Tjeng, and A. Severing, Phys. Rev. B **80**, 115106 (2009)

[30] L. Sun and Q. Wu, Rep. Prog. Phys. **79**, 084503 (2016)

[31] J. Effantin, J. Rossat-Mignod, P. Burlet, H. Bartholin, S. Kunii, and T. Kasuya, J. Magn. Magn. Mater. **47-48**, 145 (1985)

[32] M. Sundermann, K. Chen, H. Yavaş, H. Lee, Z. Fisk, M.W. Haverkort, L.H. Tjeng, and A. Severing, Europhys. Lett. **117**, 17003 (2017)

[33] W. Erkelens, L. Regnault, P. Burlet, J. Rossat-Mignod, S. Kunii, and T. Kasuya, J. Magn. Magn. Mater. **63-64**, 61 (1987)

[34] R. Shiina, H. Shiba, and P. Thalmeier, J. Phys. Soc. Jpn. **66**, 1741 (1997)

[35] A. Akbari and P. Thalmeier, Phys. Rev. Lett. **108**, 146403 (2012)

[36] S.W. Lovesey, J. Phys.: Condens. Matter **14**, 4415 (2002)

[37] T. Matsumura, T. Yonemura, K. Kunimori, M. Sera, and F. Iga, Phys. Rev. Lett. **103**, 017203 (2009)

[38] G. Friemel, Y. Li, A. Dukhnenko, N. Shitsevalova, N. Sluchanko, A. Ivanov, V. Filipov, B. Keimer, and D. Inosov, Nat. Commun. **3**, 830 (2012)

[39] P.Y. Portnichenko, S.V. Demishev, A.V. Semeno, H. Ohta, A.S. Cameron, M.A. Surmach, H. Jang, G. Friemel, A.V. Dukhnenko, N.Y. Shitsevalova, V.B. Filipov, A. Schneidewind, J. Ollivier, A. Podlesnyak, and D.S. Inosov, Phys. Rev. B **94**, 035114 (2016)

[40] A.S. Cameron, G. Friemel, and D.S. Inosov, Rep. Prog. Phys. **79**, 066502 (2016)

[41] M. Neupane, N. Alidoust, I. Belopolski, G. Bian, S.-Y. Xu, D.-J. Kim, P.P. Shibayev, D.S. Sanchez, H. Zheng, T.-R. Chang, H.-T. Jeng, P.S. Riseborough, H. Lin, A. Bansil, T. Durakiewicz, Z. Fisk, and M.Z. Hasan, Phys. Rev. B **92**, 104420 (2015)

[42] A. Koitzsch, N. Heming, M. Knupfer, P.Y. Büchner, B. Portnichenko, A.V. Dukhnenko, N.Y. Shitsevalova, V.B. Filipov, L.L. Lev, V.N. Strocov, J. Ollivier, and D.S. Inosov, Nat. Commun. **7**, 10876 (2016)

[43] E. Zirngiebl, B. Hillebrands, S. Blumenröder, G. Güntherodt, M. Loewenhaupt, J.M. Carpenter, K. Winzer, and Z. Fisk, Phys. Rev. B **30**, 4052 (1984)

[44] M. Loewenhaupt, J. Carpenter, and C.-K. Loong, J. Magn. Magn. Mater. **52**, 245 (1985)

[45] C. Terzioglu, D.A. Browne, R.G. Goodrich, A. Hassan, and Z. Fisk, Phys. Rev. B **63**, 235110 (2001)

[46] N. Sato, S. Kunii, I. Oguro, T. Komatsubara, and T. Kasuya, J. Phys. Soc. Jpn. **53**, 3967 (1984)

[47] F. Givord, J.-X. Boucherle, P. Burlet, B. Gillon, and S. Kunii, J. Phys.: Condens. Matter **15**, 3095 (2003)

[48] K. Tanaka and Y. Onuki, Acta Cryst. B **58**, 423 (2002)

[49] R. Makita, K. Tanaka, Y. Onuki, and H. Tatewaki, Acta Cryst. B **63**, 683 (2007)

[50] M.W. Haverkort, J. Phys.: Conf. Ser. **712**, 012001 (2016)

[51] A. Menth, E. Buehler, and T.H. Geballe, Phys. Rev. Lett. **22**, 295 (1969)

[52] R.L. Cohen, M. Eibschütz, and K.W. West, Phys. Rev. Lett. **24**, 383 (1970)

[53] J.W. Allen, B. Batlogg, and P. Wachter, Phys. Rev. B **20**, 4807 (1979)

[54] B. Gorshunov, N. Sluchanko, A. Volkov, M. Dressel, G. Knebel, A. Loidl, and S. Kunii, Phys. Rev. B **59**, 1808 (1999)

[55] P.S. Riseborough, Adv. Phys. **49**, 257 (2000)

[56] M. Dzero, K. Sun, V. Galitski, and P. Coleman, Phys. Rev. Lett. **104**, 106408 (2010)

[57] T. Takimoto, J. Phys. Soc. Jpn. **80**, 123710 (2011)

[58] M. Dzero, K. Sun, P. Coleman, and V. Galitski, Phys. Rev. B **85**, 045130 (2012)

[59] F. Lu, J. Zhao, H. Weng, Z. Fang, and X. Dai, Phys. Rev. Lett. **110**, 096401 (2013)

[60] M. Dzero and V. Galitski, J. Exp. Theo. Phys. **117**, 499 (2013)

[61] V. Alexandrov, M. Dzero, and P. Coleman, Phys. Rev. Lett. **111**, 226403 (2013)

[62] K. Flachbart, K. Gloos, E. Konovalova, Y. Paderno, M. Reiffers, P. Samuely, and P. Švec, Phys. Rev. B **64**, 085104 (2001)

[63] N. Xu, X. Shi, P.K. Biswas, C.E. Matt, R.S. Dhaka, Y. Huang, N.C. Plumb, M. Radović, J.H. Dil, E. Pomjakushina, K. Conder, A. Amato, Z. Salman, D.M. Paul, J. Mesot, H. Ding, and M. Shi, Phys. Rev. B **88**, 121102 (2013)

[64] Z.-H. Zhu, A. Nicolaou, G. Levy, N.P. Butch, P. Syers, X.F. Wang, J. Paglione, G.A. Sawatzky, I.S. Elfimov, and A. Damascelli, Phys. Rev. Lett. **111**, 216402 (2013)

[65] M. Neupane, N. Alidoust, S.-Y. Xu, T. Kondo, Y. Ishida, D.J. Kim, C. Liu, I. Belopolski, Y.J. Jo, T.-R. Chang, H.-T. Jeng, T. Durakiewicz, L. Balicas, H. Lin, A. Bansil, S. Shin, Z. Fisk, and M. Hasan, Nat. Commun. **4**, 2991 (2013)

[66] J. Jiang, S. Li, T. Zhang, Z. Sun, F. Chen, Z. Ye, M. Xu, Q. Ge, S. Tan, X. Niu, M. Xia, B. Xie, Y. Li, X. Chen, H. Wen, and D. Feng, Nat. Commun. **4**, 3010 (2013)

[67] J. Denlinger, J.W. Allen, J.-S. Kang, K. Sund, J.-W. Kim, J.H. Shim, B.I. Min, D.-J. Kim, and Z. Fisk, arXiv:1312.6637 (2013)

[68] J.D. Denlinger, J.W. Allen, J.-S. Kang, K. Sun, B.-I. Min, D.-J. Kim, and Z. Fisk, JPS Conf. Proc. **3**, 017038 (2014)

[69] N. Xu, P.K. Biswas, J.H. Dil, R.S. Dhaka, G. Landolt, S. Muff, C.E. Matt, X. Shi, N.C. Plumb, M. Radovic, E. Pomjakushina, K. Conder, A. Amato, S.V. Borisenko, R. Yu, H.-M. Weng, Z. Fang, X. Dai, J. Mesot, H. Ding, and M. Shi, Nat. Commun. **5**, 4566 (2014)

[70] N. Xu, C.E. Matt, E. Pomjakushina, X. Shi, R.S. Dhaka, N.C. Plumb, M. Radović, P.K. Biswas, D. Evtushinsky, V. Zabolotnyy, J.H. Dil, K. Conder, J. Mesot, H. Ding, and M. Shi, Phys. Rev. B **90**, 085148 (2014)

[71] P. Hlawenka, K. Siemensmeyer, E. Weschke, A. Varykhalov, J. Sánchez-Barriga, N.Y. Shitsevalova, A.V. Dukhnenko, V.B. Filipov, S. Gabáni, S. Flachbart, O. Rader, and E.D.L. Rienks, Nat. Commun. **9**, 517 (2018)

[72] M.M. Yee, Y. He, A. Soumyanarayanan, D.J. Kim, Z. Fisk, and J.E. Hoffman, arXiv:1308.1085 (2013)

[73] S. Rössler, T.-H. Jang, D.-J. Kim, T.L.H., Z. Fisk, and S. Steglich, F. Wirth, Proc. Natl. Acad. Science. U.S.A. **111**, 4798 (2014)

[74] W. Ruan, C. Ye, M. Guo, F. Chen, X. Chen, G.-M. Zhang, and Y. Wang, Phys. Rev. Lett. **112**, 136401 (2014)

[75] S. Rössler, L. Jiao, D.J. Kim, S. Seiro, K. Rasim, F. Steglich, L.H. Tjeng, Z. Fisk, and S. Wirth, Phil. Mag. **96**, 3262 (2016)

[76] L. Jiao, S. Rössler, D.J. Kim, L.H. Tjeng, Z. Fisk, F. Steglich, and S. Wirth, Nat. Commun. **7**, 13762 (2016)

[77] M. Ciomaga Hatnean, M.R. Lees, D.McK. Paul, and G.A. Balakrishnan, Sci. Rep. **3** 3403 (2013)

[78] X. Zhang, N.P. Butch, P. Syers, S. Ziemak, R.L. Greene, and J. Paglione, Phys. Rev. X **3**, 011011 (2013)

[79] D.J. Kim, S. Thomas, T. Grant, J. Botimer, Z. Fisk, and J. Xia, Sci. Rep. **3**, 3150 (2013)

[80] S. Wolgast, C. Kurdak, K. Sun, J.W. Allen, D.-J. Kim, and Z. Fisk, Phys. Rev. B **88**, 180405 (2013)

[81] D.J. Kim, J. Xia, and Z. Fisk, Nat. Mater. **13**, 466 (2014)

[82] S. Wolgast, Y.S. Eo, T. Öztürk, G. Li, Z. Xiang, C. Tinsman, T. Asaba, B. Lawson, F. Yu, J.W. Allen, K. Sun, L. Li, C. Kurdak, D.-J. Kim, and Z. Fisk, Phys. Rev. B **92**, 115110 (2015)

[83] S. Thomas, D.J. Kim, S.B. Chung, T. Grant, Z. Fisk, and J. Xia, Phys. Rev. B **94**, 205114 (2016)

[84] Y. Nakajima, P. Syers, X. Wang, R. Wang, and J. Paglione, Nat. Phys. **12**, 213 (2016)

[85] M. Dzero, J. Xia, V. Galitski, and P. Coleman, Annu. Rev. Condens. Matter Phys. **7**, 249 (2016)

[86] J.W. Allen, Phil. Mag. **96**, 3227 (2016)

[87] J.W. Allen, L.I. Johansson, I. Lindau, and S.B. Hagstrom, Phys. Rev. B **21**, 1335 (1980)

[88] J.M. Tarascon, Y. Ishikawa, B. Chevalier, J. Etourneau, P. Hagenmuller, and K. Kasaya, J. Physique **41**, 1141 (1980)

[89] M. Mizumaki, S. Tsutsui, and F. Iga, J. Phys.: Conf. Ser. **176**, 012034 (2009)

[90] H. Hayashi, N. Kanai, N. Kawamura, M. Mizumaki, K. Imura, N.K. Sato, H.S. Suzuki, and F. Iga, J. Anal. At. Spectrom. **28**, 373 (2013)

[91] P. Lutz, M. Thees, T.R. Peixoto, B.Y. Kang, B.K. Cho, C.H. Min, and F. Reinert, Phil. Mag. **96**, 3307 (2016)

[92] N.P. Butch, J. Paglione, P. Chow, Y. Xiao, C.A. Marianetti, C.H. Booth, and J.R. Jeffries, Phys. Rev. Lett. **116**, 156401 (2016)

[93] Y. Utsumi, D. Kasinathan, K.-T. Ko, S. Agrestini, M.W. Haverkort, S. Wirth, Y.-H. Wu, K.-D. Tsuei, D.-J. Kim, Z. Fisk, A. Tanaka, P. Thalmeier, and L.H. Tjeng, Phys. Rev. B **96**, 155130 (2017)

[94] M. Sundermann, H. Yavaş, K. Chen, D.J. Kim, Z. Fisk, D. Kasinathan, M.W. Haverkort, P. Thalmeier, A. Severing, and L.H. Tjeng, Phys. Rev. Lett. **120**, 016402 (2018)

[95] K. Lea, M. Leask, and W. Wolf, J. Phys. Chem. Sol. **23**, 1381 (1962)

[96] W.T. Fuhrman, J. Leiner, P. Nikolić, G.E. Granroth, M.B. Stone, M.D. Lumsden, L. DeBeer-Schmitt, P.A. Alekseev, J.-M. Mignot, S.M. Koohpayeh, P. Cottingham, W.A. Phelan, L. Schoop, T.M. McQueen, and C. Broholm, Phys. Rev. Lett. **114**, 036401 (2015)

[97] P. Nyhus, S.L. Cooper, Z. Fisk, and J. Sarrao, Phys. Rev. B **52**, R14308 (1995)

[98] P. Nyhus, S.L. Cooper, Z. Fisk, and J. Sarrao, Phys. Rev. B **55**, 12488 (1997)

[99] B. Frick and M. Loewenhaupt, Z. Phys. B **63**, 213 (1986)

[100] M. Loewenhaupt and M. Prager, Z. Phys. B **62**, 195 (1986)

[101] S. Sen Gupta, J.A. Bradley, M.W. Haverkort, G.T. Seidler, A. Tanaka, and G.A. Sawatzky, Phys. Rev. B **84**, 075134 (2011)

[102] P.P. Baruselli and M. Vojta, Phys. Rev. Lett. **115**, 156404 (2015)

[103] M. Legner, A. Rüegg, and M. Sigrist, Phys. Rev. Lett. **115**, 156405 (2015)

[104] P.P. Baruselli and M. Vojta, Phys. Rev. B **93**, 195117 (2016)

[105] A. Yanase and H. Harima, Prog. Theor. Phys. Suppl. **108**, 19 (1992)

[106] V.N. Antonov, B.N. Harmon, and A.N. Yaresko, Phys. Rev. B **66**, 165209 (2002)

[107] C.-J. Kang, J. Kim, K. Kim, J. Kang, J.D. Denlinger, and B.I. Min, J. Phys. Soc. Jpn. **84**, 024722 (2015)

[108] G. Sawatzky, in E. Pavarini, E. Koch, J. van den Brink and G. Sawatzky (eds.): *Quantum Materials: Experiments and Theory*, Modeling and Simulation Vol. 6 (Forschungszentrum Jülich, 2016)